J|A|C|S ARTICLES

Published on Web 11/16/2009

Role of Self-Organization, Nanostructuring, and Lattice Strain on Phonon Transport in $NaPb_{18-x}Sn_xBiTe_{20}$ Thermoelectric Materials

Jiaqing He,[†,‡] Aurelie Gueguen,[‡] Joseph R. Sootsman,[‡] Jin-cheng Zheng,[§] Lijun Wu,[||] Yimei Zhu,[||] Mercouri G. Kanatzidis,[*,‡,⊥] and Vinayak P. Dravid[*,†]

Department of Materials Science & Engineering, Northwestern University, Evanston, Illinois 60208, Department of Chemistry, Northwestern University, Evanston, Illinois 60208, Department of Physics, and Institute of Theoretical Physics and Astrophysics, Xiamen University, Xiamen 361005, People's Republic of China, Condensed Matter Physics & Materials Science Department, Brookhaven National Laboratory, Upton, New York 11973, and Materials Science Division, Argonne National Laboratory, Argonne, Illinois 60439

Received July 2, 2009; E-mail: v-dravid@northwestern.edu; m-kanatzidis@northwestern.edu

Abstract: The composition and microstructure of five thermoelectric materials, PbTe, SnTe, $Pb_{0.65}Sn_{0.35}Te$ and $NaPb_{18-x}Sn_xBiTe_{20}$ ($x = 5$, 9), were investigated by advanced transmission electron microcopy. We confirm that the pure PbTe, SnTe, and $Pb_{0.65}Sn_{0.35}Te$ have a uniform crystalline structure and homogeneous compositions without any nanoscale inclusions. On the other hand, the nominal $NaPb_9Sn_9BiTe_{20}$ phase contains extensive inhomogeneities and nanostructures with size distribution of 3−7 nm. We find that the chemical architecture of the $NaPb_{13}Sn_5BiTe_{20}$ member of the series to be more complex; besides nanoscale precipitates, self-organized lamellar structures are present which were identified as PbTe and SnTe by composition analysis and transmission electron microscopy image simulations. Density functional theory calculations suggest that the arrangement of the lamellar structures conforms to the lowest total energy configuration. Geometric-phase analyses revealed large distributed elastic strain around the nanoscale inclusions and lamellar structures. We propose that interface-induced elastic perturbations in the matrix play a decisive role in affecting the phonon-propagation pathways. The interfaces further enhance phonon scattering which, in turn, reduces the lattice thermal conductivity in these systems that directly results directly in improvement in the thermoelectric figure of merit.

Introduction

Thermoelectric materials are being explored for various energy supply and conservation applications.[1,2] Traditional bulk thermoelectric (TE) materials typically do not display a very high figure of merit (ZT) at operating temperatures that satisfies the economic market demand.[3] The figure of merit for TE is defined as follows:

$$\mathrm{ZT} = \frac{S^2 T}{\kappa \rho}$$

where S, σ, κ, and T are the Seebeck coefficient, electrical conductivity, thermal conductivity, and absolute temperature, respectively.[4] The thermal conductivity comprises the combination of heat carried by phonons or lattice vibrations (κ_{lat}), and electrical carriers (κ_{elec}). If bulk materials with high ZT can be developed and processed inexpensively, then their applications may be realized in widespread markets for power generators and refrigeration.[5] An established way to improve ZT is to lower the lattice thermal conductivity via solid solution alloying to create point defects and enhance phonon scattering, an approach that reduces the lattice thermal conductivity to the so-called "alloy limit". This approach has its maximum impact at room temperature and below but is less effective at higher temperatures. A new concept has emerged involving the introduction of nanostructures in the thermoelectric matrix that has resulted in much lower thermal conductivities, which are well below the alloy limit. The many synthetic techniques proposed for introducing these inclusions are the fabrication of superlattices,[6,7] quantum dots,[8] nanocrystalline inclusions,[9−12] and promoting self-assembly,[13] as well the possibilities of exploring new structures.[14] The first two methods have claimed to improve the materials' ZT because they diminish thermal conductivity by phonon scattering at the interfaces of nanoscale. However, recent thermal conductivity measurements of PbTe-PbSe nano-

[†] Department of Materials Science & Engineering, Northwestern University.
[‡] Department of Chemistry, Northwestern University.
[§] Department of Physics, and Institute of Theoretical Physics and Astrophysics, Xiamen University.
[||] Condensed Matter Physics & Materials Science Department, Brookhaven National Laboratory.
[⊥] Materials Science Division, Argonne National Laboratory.

(1) Sales, B. C. *Science* **2002**, *295*, 1248–1249.
(2) Disalvo, F. J. *Science* **1999**, *285*, 703–706.
(3) Tritt, T. M.; Subramanian, M. A. *MRS Bull.* **2006**, *31*, 113.
(4) Rowe, D. M. *CRC Handbook of Thermoelectrics*; CRC Press: Boca Raton, FL 1995, 701.
(5) Yang, J.; Caillat, T. *MRS Bull.* **2006**, *31*, 224–229.
(6) Venkatasubramanian, R.; Siivola, R. E.; Colpitts, T.; Oquinn, B. *Nature* **2001**, *413*, 597–602.
(7) Venkatasubramanian, R.; Colpitts, T.; Oquinn, B.; Liu, S.; Ei-Masry, N.; Lamvik, M. *Appl. Phys. Lett.* **1999**, *75*, 1104–1106.

 10.1021/ja905448b CCC: $40.75

scale superlattice structures were reported to be higher than previously estimated,[15] thereby casting some doubt on the low thermal conductivity of such artificial structures. It is challenging to find new superlattice materials that will be stable at high temperature given the complexity of multicomponent phase equilibria. This situation has prompted the exploration of new methods to prepare *bulk* nanostructured and/or self-organized lamellar structured materials, wherein the majority of acoustic phonons are scattered most effectively by nanoscale features. For the case of PbTe, such materials have been generated through metallurgical processes, such as matrix encapsulation,[16] spinodal decomposition,[17] and nucleation and growth,[18] thus potentially amenable to scale-up processes.

The *n*-type high ZT TE materials $AgPb_mSbTe_{2+m}$ (LAST) have been extensively studied by transmission electron microscopy (TEM).[19,20] The substitution of Sn for Pb in such systems results in a more complex system that contains five different elements and exhibits very low lattice thermal conductivities. This results in *p*-type behavior with a high ZT $\approx$ 1.5. Here, employing TEM, for the first time we have undertaken a detailed study of the nanostructures found in the group of $NaPb_{18-x}Sn_xBiTe_{20}$ materials which derive from the high thermoelectric performance materials family of *p*-type $NaPb_mSbTe_{2+m}$. The main reason for the high ZT ($\sim$1.3 at 670 K) observed in $NaPb_{18}BiTe_{20}$ is the extremely low lattice thermal conductivity ($\sim$0.5 W/mK at 670 K). We demonstrate that the nature and character of nanoscale inclusions, interfaces, and associated lattice strains have profound yet predictable influence on their thermoelectric properties. For this study, we have selected the recently described complex thermoelectric materials $NaPb_{18-x}Sn_xBiTe_{20}$ ($x = 5, 9$),[21] with their desirable features of slow solidification and decomposition, to obtain readily observable self-organized lamellar structures and nanoscale precipitates. These materials were investigated by TEM to elucidate the relationship between lattice thermal conductivity and the nanoscale features and architecture. We compare and contrast our findings directly with those obtained from the basic archetypal thermoelectric materials PbTe (a narrow gap semiconductor), SnTe (a semimetal), and $Pb_{1-x}Sn_xTe$ (their alloy). We show that the latter basic systems are not nanostructured and we attribute the significantly lower thermal conductivity of the nanostructured $NaPb_{18-x}Sn_xBiTe_{20}$ to the extensive presence of lattice strain at the nanoscale precipitate−matrix interface.

Experimental Procedure

The samples $NaPb_{18-x}Sn_xBiTe_{20}$ ($x = 5, 9$) were prepared as polycrystalline ingots in silica tubes by mixing high-purity Na (Aldrich, 99.95%), Pb and Sn (Rotometals, 99.99%), Bi (Bismuth, 99.999%), and Te (Plasmaterials, 99.999%) in the appropriate stoichiometric ratio.[21] To prevent reaction between the sodium metal and silica, the tubes were carbon-coated prior to use. All components (except Na) were loaded into silica tubes under ambient atmosphere and the corresponding amount of Na was later added under inert atmosphere in a dry glovebox. The silica tubes were then flame-sealed under a residual pressure of $\sim 1 \times 10^{-4}$ Torr, placed into a tube furnace (mounted on a rocking table), and heated at 1250 K for 4 h to allow complete melting of all components. While molten, the furnace was allowed to rock for 2 h to facilitate complete mixing and homogeneity of the liquid phase. The furnace was finally immobilized at the vertical position and was cooled from 1250 to 820 K over 43 h followed by a faster cool (6−8 h) to room temperature. The resulting ingots generally were silvery-metallic in color with a smooth surface.

The samples first were examined by powder X-ray diffraction, scanning electron microscopy, and their electrical-transport properties and thermal conductivity measured,[21] then, they were investigated under the JEOL 2100F and 3000F TEMs. TEM samples were prepared by conventional standard methods. The samples were cut into 3 mm-diameter discs by disk cutter, then ground, dimpled, polished, and subsequently Ar-ion milled on a stage cooled with liquid nitrogen. High-resolution images were simulated with the Mac Tempas program code with the following parameters as input: Spherical aberration of 1 mm, defocus spread of 8 nm, semiconvergence angle of illumination of 0.55 mrad, and a 7 nm^{-1} diameter of the objective lens' aperture.

Results and Discussion

In Figure 1, we compare the electrical-transport properties of the five samples: PbTe, SnTe, $Pb_{0.6}Sn_{0.4}Te$,[22] $NaPb_{13}Sn_5BiTe_{20}$ and $NaPb_9Sn_9BiTe_{20}$. The electrical conductivity of SnTe invariably is higher than that of the others (Figure 1a) because of the high amount of naturally occurring vacancies in the Sn sublattice that greatly increases the carrier concentration to nearly metallic levels.[23,24] This is the reason for the very low Seebeck coefficient (Figure 1b) of the SnTe sample compared to that of the $NaPb_{18-x}Sn_xBiTe_{20}$ ($x = 5, 9$) samples. Expectedly, the total thermal conductivity (Figure 1c) of the SnTe sample[25] is much higher than that of the other four samples; $NaPb_{13}Sn_5BiTe_{20}$ has the lowest value, and the probable reason for this is discussed later.

To clarify the underlying mechanism of thermal conductivity in the $NaPb_{18-x}Sn_xBiTe_{20}$ ($x = 5, 9$) samples, we undertook a TEM investigation of the internal microstructure of the samples. Figure 2, parts (a), (b), and (e), shows the low magnification images of PbTe, $Pb_{0.65}Sn_{0.35}Te$, and $NaPb_9Sn_9BiTe_{20}$, respectively. Figure 2(a) reveals the homo-

(8) Harman, T. C.; Taylor, P. J.; Walsh, M. P.; LaForge, B. E. *Science* **2002**, *297*, 2229–2232.
(9) Quarez, E.; Hsu, K. F.; Pcionek, R.; Frangis, N.; Polychroniadis, E. K.; Kanatzidis, M. G. *J. Am. Chem. Soc.* **2005**, *127*, 9177–9190.
(10) Hsu, K. F.; Loo, S.; Guo, F.; Chen, W.; Dyck, J. S.; Uher, C.; Hogan, T. P.; Kanatzidis, M. G. *Science* **2004**, *303*, 818–821.
(11) Poudeu, P. F. R.; D'Angelo, J.; Downey, A. D.; Short, J. L.; Hogan, T. P.; Kanatzidis, M. G. *Angew. Chem., Int. Ed.* **2006**, *45*, 3835–3839.
(12) Androulakis, J.; Hsu, K. F.; Pcionek, R.; Kong, H.; Uher, C.; Dangelo, J. J.; Downey, A. D.; Hogan, T. P.; Kanatzidis, M. G. *Adv. Mater.* **2006**, *18*, 1170–1173.
(13) Ikeda, T.; Collins, L. A.; Ravi, V. A.; Gascoin, F. S.; Haile, S. M.; Snyder, G. J. *Chem. Mater.* **2007**, *19*, 763–767.
(14) Kanatzidis, M. G. *Acc. Chem. Res.* **2005**, *38*, 359–368.
(15) Koh, Y. K.; Vineis, C. J.; Calawa, S. D.; Walsh, M. P.; Cahill, D. G. *Appl. Phys. Lett.* **2009**, *94*, 153101.
(16) Sootsman, J. R.; Pcionek, R. J.; Kong, H. J.; Uher, C.; Kanatzidis, M. G. *Chem. Mater.* **2006**, *18*, 4993–4995.
(17) Androulakis, J.; Lin, C. H.; Kong, H. J.; Uher, C.; Wu, C.; Hogan, T.; Cook, B. C.; Caillat, T.; Paraskevopoulos, K. M. *J. Am. Chem. Soc.* **2007**, *192*, 9780–9788.
(18) Heremans, J. P.; Thrush, C. M.; Morelli, D. T. *J. Appl. Phys.* **2005**, *98*, 063703.
(19) Wu, L.; Zheng, J.-C.; Zhou, J.; Li, Q.; Yang, J.; Zhu, Y. *J. Appl. Phys.* **2009**, *105*, 094317.
(20) Cook, B. A.; Cramer, M. J.; Harringa, J. L.; Han, M. K.; Chung, D. Y.; Kanatzidis, M. G. *Adv. Funct. Mater.* **2009**, *19*, 1254–1259.
(21) Gueguen, A.; Poudeu, P.; Kong, H.; Moses, S.; Uher, C.; He, J. Q.; Dravid, V.; Paraskevopoulos, K.; Kanatzidis, M. G. *Chem. Matter.* **2009**, *21*, 1683–1694.
(22) Alekseeva, G. T.; Vedernikov, M. V.; Gurieva, E. A.; Prokof'eva, L. V.; Ravich, Y. I. *Semiconductors* **2000**, *34*, 897–901.
(23) Hemstreet, L. A. *Phys. Rev. B* **1975**, *12*, 1212–1216.
(24) Rogacheva, E. I.; Nashchekina, O. N.; Tavrina, T. V.; Vekhov, Y. O.; Sipatov, M. A. Y.; Dresselhaus, S. in *1st International Symposium on Point Defect and Stoichiometry*, Sendai, JAPAN, 2003, pp 497.
(25) Vedeneev, V. P.; Krivoruchko, S. P.; Sabo, E. P. *Semiconductors* **1998**, *32*, 241–244.

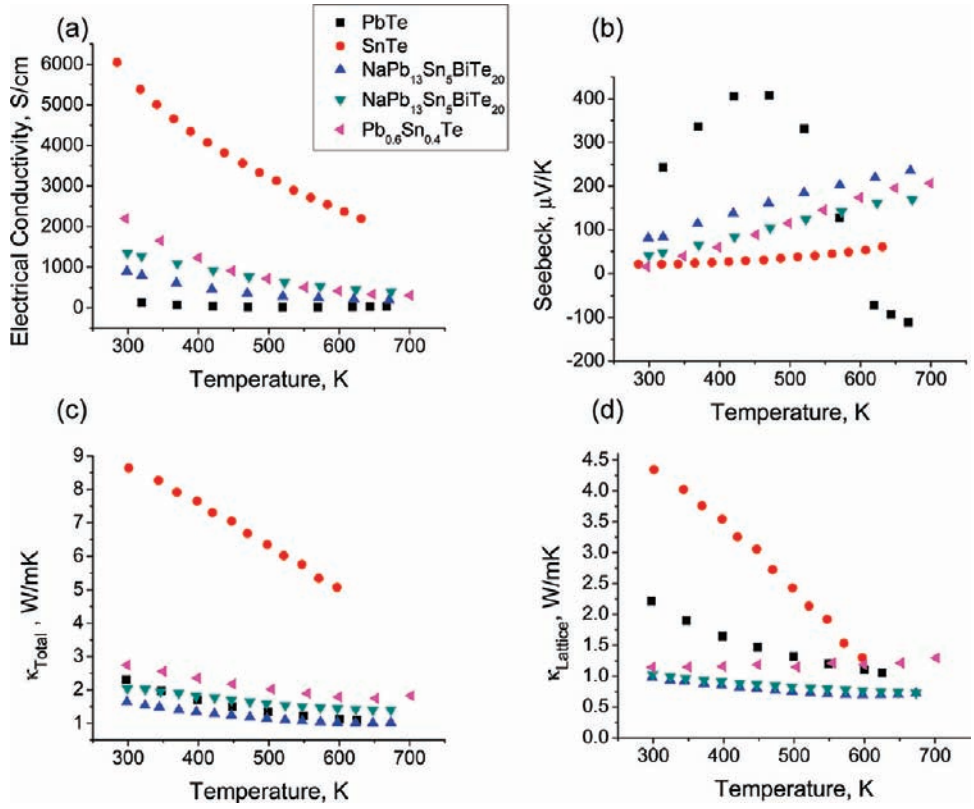

Figure 1. (a) Electrical conductivity, (b) Seebeck coefficient, (c) total thermal conductivity, and (d) lattice thermal conductivity dependence of temperature of five samples, PbTe, SnTe, $Pb_{0.6}Sn_{0.4}Te$, $NaPb_{13}Sn_5BiTe_{20}$, and $NaPb_9Sn_9BiTe_{20}$.

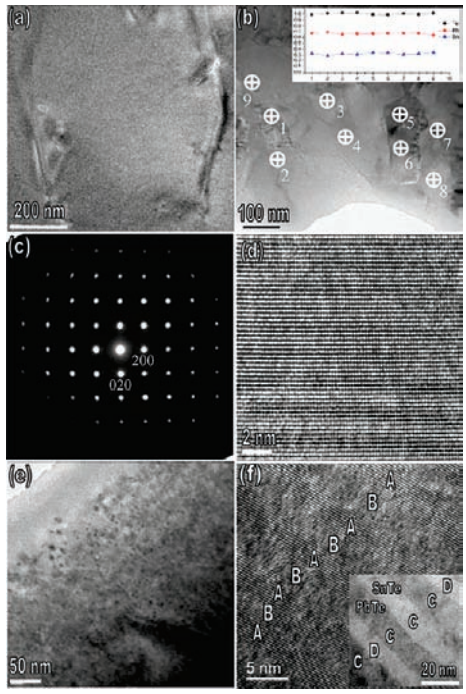

Figure 2. Low-magnification images of three samples PbTe (a), $Pb_{0.65}Sn_{0.35}Te$ (b), $NaPb_9Sn_9BiTe_{20}$ (e). Electron diffraction pattern (c) and lattice image (d) of sample $Pb_{0.65}Sn_{0.35}Te$. (f) Two kinds of lamellar structures of $NaPb_{13}Sn_5BiTe_{20}$. PbTe and $Pb_{0.65}Sn_{0.35}Te$ have no precipitates, $x = 9$ shows only the inclusions, and $x = 5$ shows lamellar structures and inclusions.

geneity of the PbTe material that lacks any precipitates; some contrast features in the image reflect the presence of dislocations and stacking faults. SnTe (not shown) displays a similar homogeneous composition and microstructure. Figure 2(b), one bright field image of $Pb_{0.65}Sn_{0.35}Te$, depicts some nonuniform contrast, which are mainly due to the point defects and grain boundaries. There is no evidence of nanoscale precipitates or lamellar structures in the $Pb_{0.65}Sn_{0.35}Te$ sample. Energy Dispersive X-ray Spectroscopy (EDS) data (insert) of different positions show uniform composition, with stoichiometric $Pb_{0.661(5)}Sn_{0.337(6)}Te_{1.002(3)}$. In Figure 2(c), electron diffraction of $Pb_{0.65}Sn_{0.35}Te$ with an aperture including a large number of crystal grains does not show extra diffraction spots besides from $Pb_{0.65}Sn_{0.35}Te$. Only some high order spots are elongated due to a small fraction of in-plane misaligned grains. Figure 2(d), a typical lattice image of $Pb_{0.65}Sn_{0.35}Te$, does not show any nanoscale precipitates. Therefore, $Pb_{0.65}Sn_{0.35}Te$ is clearly a solid solution and confirms the long held belief that the $Pb_{1-x}Sn_xTe$ system is a solid solution.[26−28]

In contrast to the basic parent materials above, Figure 2(e), a representative image of the $NaPb_9Sn_9BiTe_{20}$ sample, shows two typical features; one close to the edge of the image, displaying very uniform contrast due to beam damage, while the other, about 80 nm away from the edge, contains many regular precipitates with dark contrast, in the range of 2−10 nm. Interestingly, the $NaPb_{13}Sn_5BiTe_{20}$ sample often contained two different kinds of lamellar structures, in addition to the regular precipitates (similar to those in Figure 2e). The first type, shown in Figure 2(f), a high-magnification lattice image of the lamellar structure, clearly reveals ordered modulated structures labeled sequence ABAB...with a (100) interface plane. The

(26) Wagner, J. W.; Woolley, J. C. *Mater. Res. Bull.* **1967**, *2*, 1055–1062.
(27) Laugier, A. *Rev. Phys. Appl.* **1973**, *8*, 259–270.
(28) Kattner, U.; Lukas, H. L.; Petzow, G.; Gather, B.; Irle, E.; Blachnik, R. *Z. Metallkd.* **1988**, *79*, 32–40.

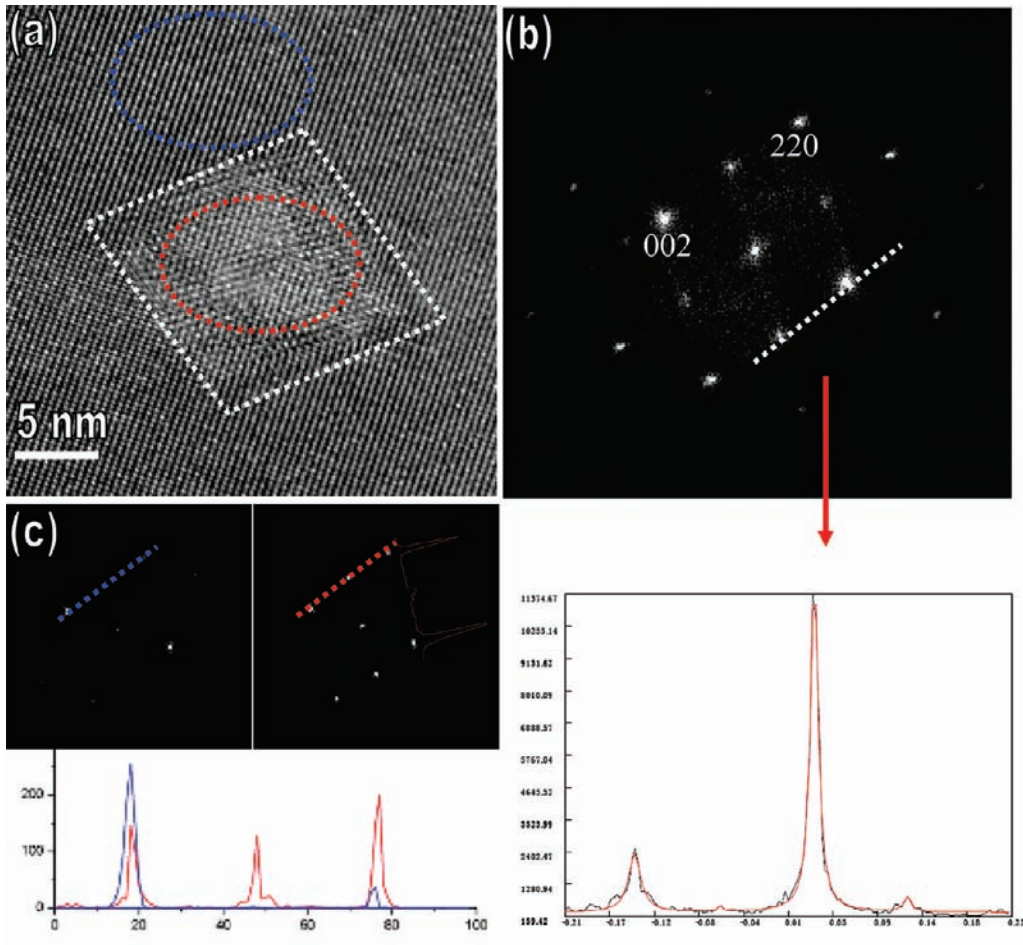

Figure 3. (a) Lattice image of $NaPb_{13}Sn_5BiTe_{20}$ with nanoscale inclusions. (b) FFT images of the whole image including the matrix and precipitate; the line scanning profile did not show split speaks. (c) FFT images of the precipitate and of the matrix, and the intensity profile. Apparently, the superlattice arises from the precipitates only. For clarity, the intensity profiles of line scan across the Bragg and superlattice reflections (marked as red solid line) are included in one image.

secondary type inserted in Figure 2(f) illustrates one type with sequence CDCDCD... These dark and bright-contrast lamellar structures, 100−200 nm wide, grow along the (112) plane. EDS showed that the level of Pb is high in regions marked by A and C, while areas denoted by B and D are rich in Sn, implying local nanoscale segregation between the two phases PbTe and SnTe.

To grasp the relationship between physical properties and nanoscale precipitates and lamellar structures, we have extensively investigated their microstructures. Figure 3(a) is a high resolution transmission electron microscopy (HRTEM) image of a $NaPb_{13}Sn_5BiTe_{20}$ sample that shows one rhombic-shaped precipitate inserted in the matrix. Figure 3(b) depicts the Fast Fourier Transforms (FFTs) of the whole image in (a), and a line-scanning profile crossing the strong and weak peaks. No split peaks were observed, signifying that there are "identical" lattice parameters or minimal mismatch between the matrix and precipitates. Figure 3(c) contains the FFT images of two regions [precipitate (red oval) and matrix (blue oval)] in Figure 3(a), which indicate additional superlattice spots arising from the precipitates. The line profile, encompassing the precipitates and matrix, demonstrates that the peak spot arises only from the precipitate; therefore, the lattice parameters of precipitates are twice those of the matrix. Adopting the lattice parameter of the matrix, 0.635 nm (X-ray diffraction data from ref 21) as the standard, the precipitate lattice constant is estimated to be ∼1.270 nm. We can infer that the precipitates also belong to the nominal cubic structure. Similar to the structures of precipitates in previously reported LAST system,[9] the precipitates here are probably nominally $NaPb_2BiTe_4$.

Therefore, we believe that our experimental work indicates two types of nanoscale inclusions; one with similar lattice parameters as the matrix, resulting in minimal misfit strain at the boundary between matrix and nanoscale inclusions, and with different composition (see above), another has both lattice distortions and different composition (see later). The first type of nanoscale inclusions will likely exhibit only mass-contrast scattering of the phonons, however, the second type of precipitate will, in addition, result in the scattering of phonons by interfacial strain.

Figure 4(a) is an HRTEM image showing the lamellar structure and precipitates. Figure 4(b) is its FFT pattern and line profile across two spots (002) and (220), each of which display three clear spot-splittings. After applying the Lorentzian fit function[19] to all of the split peaks, we have refined the lattice parameters of all of the phases; (i.e., the out-of-plane lattice parameters of PbTe, SnTe, and the precipitate, respectively, as 0.6487, 0.5984, and 0.5660 nm). Similarly, the in-plane values were derived as 0.6165, 0.5925, and 0.5773 nm. Figure 4(c) shows enlargements of the lattice images in Figure 4(a) indicating that the modulated intensity contrast is based on two phases, PbTe and SnTe. Figure 4(d) is the proposed atomic

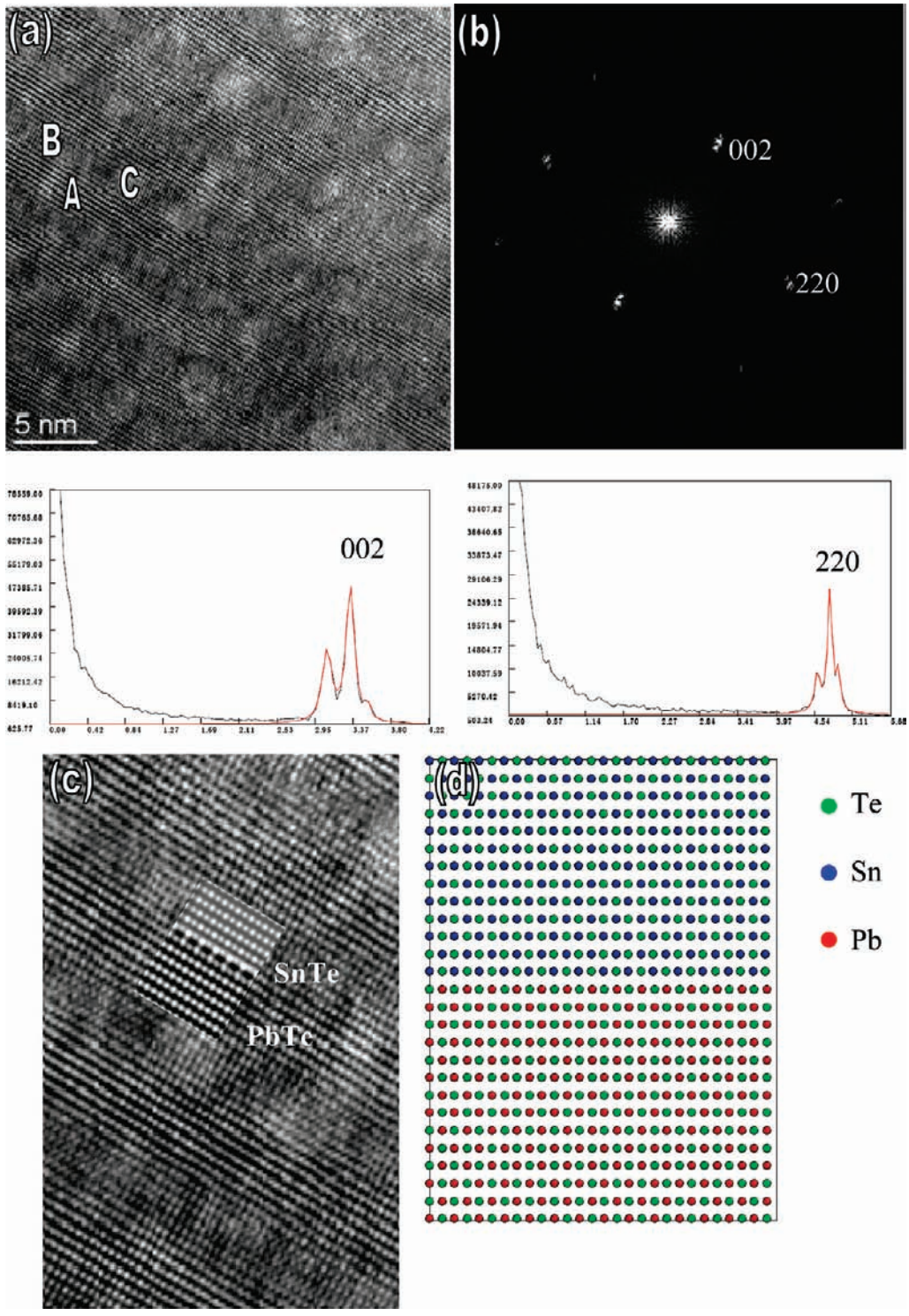

Figure 4. (a) Lattice image of $NaPb_{13}Sn_5BiTe_{20}$ including lamellar structure and precipitates, (b) the FFT image and two line scanning profiles crossing the 002 and 220 peaks, respectively. Each peak shows three split peaks. (c) One enlarged lattice image from (a). (d) Modeling based on SnTe and PbTe, and the simulated image, well match the experimental findings.

model of one interface including the PbTe and SnTe phases. The simulated high-resolution image (insert Figure 4c) incorporating the proposed model matches well with the experimental image, confirming the general validity of the proposed atomic structure of the interface.

As is well-known, phonon scattering is related to the distribution of strain around the precipitates and lamellar structures.[29,30] The derivation of local semiquantitative strain[31,32] is reflected in Figures 5 and 6, for inclusion and lamellar structures, respectively. Figure 5(a) shows the lattice image of

(29) Carruthers, P. *Phys. Rev.* **1959**, *114*, 995–1001.
(30) Carruthers, P. *Rev. Mod. Phys.* **1961**, *33*, 92–138.
(31) Hytch, M. J.; Snoeck, E.; Kilaas, R. *Ultramicroscopy* **1998**, *74*, 131–146.
(32) He, J. Q.; Vasco, E.; Jia, C. L.; Wang, R. H. *Appl. Phys. Lett.* **2005**, *87*, 062901.

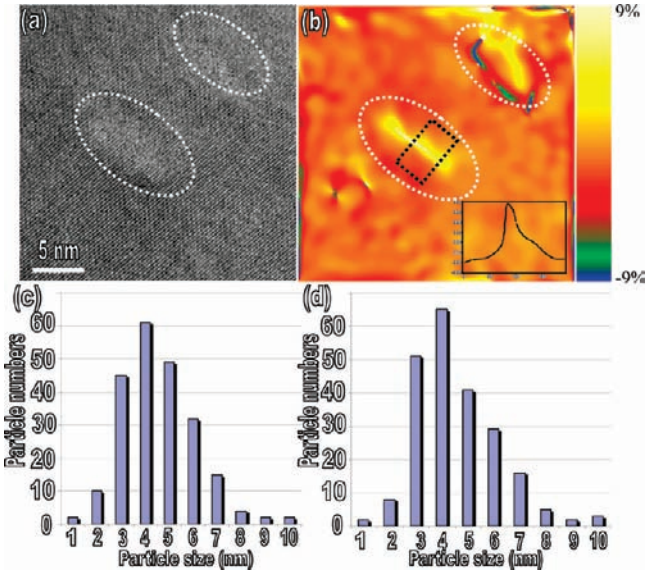

Figure 5. (a) High-magnification lattice image of the nanoscale inclusions in $NaPb_{13}Sn_5BiTe_{20}$. (b) The strain distribution of the nanoscale inclusions. Parts (c) and (d) are the size distributions of nanoscale inclusions in $NaPb_{13}Sn_5BiTe_{20}$ and $NaPb_9Sn_9BiTe_{20}$, respectively.

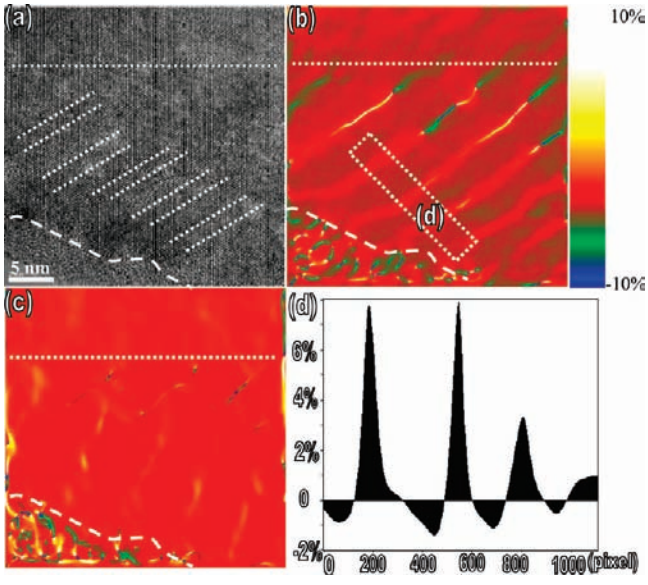

Figure 6. (a) High-magnification HRTEM image of $NaPb_{13}Sn_5BiTe_{20}$ with a nonlamellar structural region, lamellar structural region, and amorphous region. Parts (b) and (c) are the strain maps along out-of-plane and in-plane, respectively. (d) The line scanning profile of the marked region in Figure 5(b), showing the 6% off between the lattice parameters of SnTe and PbTe.

the $NaPb_{13}Sn_5BiTe_{20}$ sample, with inclusions of two different sizes. The findings from our geometric phase-analysis (Figure 5(b))[30,31] disclose large strains at the boundaries between the matrix and inclusions. Figure 5, parts (c) and (d), shows histograms of the distributions of the grain size of the inclusions in sample $x = 5$ and $x = 9$, respectively; and are very similar. We note that if the boundaries of the precipitates are not regular, then the grain sizes that are included in the calculations are based on the proportional square root of their area. We see that in both $NaPb_{13}Sn_5BiTe_{20}$ and $NaPb_9Sn_9BiTe_{20}$, the nanostructures range between 3−7 nm.

Figure 6 provides details of the strain analysis of the main kind of lamellar structure in $NaPb_{13}Sn_5BiTe_{20}$. Figure 6a is a lattice image that covers three regions: A, close to the edge amorphous-like region; B, the lamellar structure region; and, C, the nonlamellar structure region. Figure 6, parts (b) and (c), displays strain maps along the 001- and 110-directions, respectively. Three distinct regions are seen in Figure 6(b): (1) A is an amorphous-like region, in which the irregular contrast represents damage from the ion beam thinning; (2) B is an area displaying very regular lamellar structures (the line-scanning profile in part d shows that, on average, there is a separation of about 6% off between PbTe and SnTe along [100]); and, (3) C is a region of nonlamellar structure with homogeneous contrast. However, except for region A in Figure 6c, regions B and C exhibit uniform contrast, suggesting lattice match between PbTe and SnTe along [110]. These finding signify that SnTe is highly distorted at the interfaces, which is different from Figure 4 with a mixture of precipitates and lamellar structures. At room temperature, PbTe and SnTe have NaCl-type cubic crystal structure, with lattice parameters of 0.6462 and 0.6331 nm, respectively. Because the interatomic bonding in PbTe is stronger than that in SnTe,[33] we regard the in-plane lattice parameter of PbTe at 0.6462 nm to essentially remain fixed in space, while that of SnTe to experience tensile strain. The lattice mismatch parameter along the out-of-plane direction is $(0.6331^3/0.6462^2$ nm-0.6462 nm$)/0.6462$ nm $= -5.96\%$. The calculated value is in close agreement with the experimental data.

Although our examination of the $NaPb_{13}Sn_5BiTe_{20}$ specimens has revealed two kinds of lamellar structures, the lamellae with {100} interfacial planes between the PbTe and SnTe phases appear to dominate over the entire sample. In order to understand this phenomenon, we resorted to first-principles pseudopotential calculations within the local-density functional theory (DFT)[34] for interface energetics for PbTe-SnTe, as well as the surfaces of PbTe and SnTe in different orientations. The geometries of the systems are fully relaxed in order to achieve the optimized structure. Usually, we regard the formation energy as the sum of the interfacial energy and strain energy, and the formation energy (eV/atom) of $(PbTe)_n/(SnTe)_n$ superlattices can be expressed as follows:[35]

$$E_{\text{form}}(\text{per} - \text{atom}) = [E_{\text{tot}}^{(\text{PbTe})_n/(\text{SnTe})_n} - (E_{\text{tot}}^{\text{PbTe}} + E_{\text{tot}}^{\text{SnTe}})n]/4n$$

The calculated formation energy for a $(PbTe)_n/(SnTe)_n$ superlattice is found to be ∼5 meV/atoms for different orientations, namely, (100), (110), and (111) with $n > 2$. The small formation energy is in good agreement with the fact that there is complete miscibility in this system to form the well-known solid solution alloy of PbTe-SnTe (as we have shown above).

We notice, however, that for the (111) alignment, the formation energy of $(PbTe)_1/(SnTe)_1$ is almost the same as that of $(PbTe)_n/(SnTe)_n$ superlattice with large n, while for (100) or (110) orientations, the formation energy of $(PbTe)_1/(SnTe)_1$ is about 6 meV/atom, which is slightly larger than that of $(PbTe)_n/(SnTe)_n$ superlattice with $n > 2$. This implies that for (100) or (110) orientations, there is higher possibility to form $(PbTe)_n/(SnTe)_n$ superlattice with large n, compared to (111) orientation, from the energetic point of view. Because the formation energies

(33) Gelbstein, Y.; Gotesman, G.; Lishzinker, Y.; Dashevsky, Z.; Dariel, M. P. *Scr. Mater.* **2008**, *58*, 251–254.
(34) The DFT calculations are performed using first-principles pseudopotential plane-wave method, as implemented in the QUANTUM ESPRESSO package (Baroni S., http://www.pwscf.org/).
(35) Zheng, J. C.; Wang, H. Q.; Wee, A. T. S.; Huan, C. H. A. *Phys. Rev. B* **2002**, *66*, 092104.

Table 1. Calculated Surface Energies of PbTe and SnTe along (100), (110), and (111)

	(100) meV/Å^2	(110) meV/Å^2	(111) meV/Å^2
PbTe	22.1	31.6	48.4
SnTe	23.5	30.9	39.4

of $(PbTe)_n/(SnTe)_n$ superlattices in various orientations have relatively small difference, formation energy alone may not be the only reason for the observation of the (100) superlattices. Considering the possibility of forming nanocrystal facets or grain boundaries during the synthesis procedure, we then turn to the surface energies of PbTe and SnTe in (100), (110), and (111) orientations, in order to check the surface effects of possible facets.

The surface energy $E_{surface}$ is calculated by following formula:

$$E_{surface} = \frac{E_{slab} - E_{bulk}}{2S}$$

Here, E_{slab} is the total energy of slab, and E_{bulk} is the total energy of bulk system with the same atom numbers as in the slab calculations. S is the surface area. Since there are two surfaces in the slab, the energy difference $E_{slab} - E_{bulk}$ should be normalized by $2S$. The calculated surface energies for cubic PbTe and SnTe are listed in Table 1.

It is clearly seen that the (100) surfaces of both PbTe and SnTe have the lowest surface energies, compared to (110) and (111) surfaces. This suggests that it is more likely to form (100) facets of PbTe or SnTe if the grain boundaries are created in the ingots during the synthesis procedure. While First-Principles calculations are hardly fully deterministic given the complexity of such calculations and approximations, the results nevertheless conform to the experimental observations of lamellar structures with (100) orientations, which has a smaller surface energy and formation energy.

The consensus emerging from a wide variety of experimental results is that nanostructures are responsible for causing large reductions in the lattice thermal-conductivity of materials.[9,10,36−40] Compared to PbTe and SnTe, the considerably lower lattice thermal-conductivity observed in the $NaPb_{18-x}Sn_xBiTe_{20}$ (x = 5, 9) materials is likely caused by the presence of the observed nanoscale inclusions.

Although it is very complicated to theoretically calculate the contributions of nanoscale inclusions and lamellar structures to the lattice thermal conductivity, we can assess the difference between materials of intermetallic composition and the current case with nanostructures and lamellar structures. For the former, if we suppose that $NaPb_{18-x}SnBiTe_{20}$ has only Umklapp scattering and point defects,[41] then we can accurately calculate the lattice thermal conductivity of $NaPb_{18-x}Sn_xBiTe_{20}$.

Following the theory of Calloway et al.[41,42] for κ_L in disordered crystals at $T > \theta_D$ (Debye temperature) where phonon grain-boundary scattering may be ignored, the ratio of κ_L of the crystal with disorder to that without disorder K_L^p is as follows:

$$\frac{\kappa_L}{\kappa_L^p} = \frac{\tan^{-1}(u)}{u}, u^2 = \frac{\pi^2 \theta_D \Omega}{h\nu^2} \kappa_L^p \Gamma_{expt}$$

where u, Ω, h, ν, and Γ_{expt} are the disorder scaling parameter, the average volume/ atom, the Planck constant, the average lattice sound-velocity, and the experimental disorder scattering-parameter; respectively. The Γ_{expt} includes mass scattering, Γ_M, and strain-field fluctuation scattering, Γ_S. Following the expressions for Γ_M and Γ_S in ref 41, we obtain $\Gamma_{cal} = \Gamma_M + \Gamma_S \approx 0.0307 + 0.0377 = 0.0684$,[43] Using the experimental data from ref 21 then $u = 4.77$, which finally yields $\Gamma_{expt} = 0.556$,[43] a value much higher than the calculated figure of 0.0684.

This calculation is based on a system without nano scale inclusions; accordingly, the difference in value between our calculations and the experimental results is mainly attributed to the presence of nanostructures such as those shown in Figure 2b. Comparing samples $NaPb_{18-x}Sn_xBiTe_{20}$ $x = 5$, and $x = 9$ (Figure 4), wherein there are very similar sized precipitates, strain distributions, and volume fractions, then their lattice thermal conductivity should be comparable; however, our measurement data in Figure 1d show a 10% difference. It is not clear what role the existence of two kinds of additional lamellar structures in $NaPb_{13}Sn_5BiTe_{20}$, which experience 6% strain at the interface, plays in the overall phonon scattering; one would expect additional phonon scattering at the interfaces. The strain by coherent nature of the interfaces suggest that mobile electrons could be essentially unimpeded due to the small band offset between the adjacent layers of the lamellar structures. In principle, the lamellar structures should greatly decrease the lattice thermal conductivity; however, our physical measurements show a negligible difference. One reason for this could be a relatively low volume fraction of the lamellar structures in this sample.

From our above TEM observations, $Pb_{0.65}Sn_{0.35}Te$ is a solid solution, and $NaPb_{18-x}Sn_xBiTe_{20}$ $x = 5$, and $x = 9$ are not, show nanoscale precipitates and lamellar structures, which means that the addition $NaBiTe_2$ is responsible for the segregation. If we refine further the synthesis conditions and can generate more nanoscale inclusions and self-organized lamellar structures in this system, this may also further reduce the lattice thermal conductivity. Ikeda et al.[13] have controlled spacing and volume of the self-assembly lamellar structures in $PbTe$-Sb_2Te_3 system by the adjusting the time and/or temperature of the transformation process. We are currently testing dissimilar additions, such as $NaBiTe_2$, $AgBiTe_2$, and $NaSbTe_2$. Therefore, our synthetic approach could be applied extensively in creating superior and potentially cost-effective thermoelectric materials.

Conclusions

An integrated study using high-resolution transmission electron microcopy, geometry-phase analysis, in concert with density functional theory reveals that nanoscale precipitates and lamellar structures exist and play a major role in increasing phonon scattering and reducing lattice thermal conductivity in these PbTe-based thermoelectric materials. Our detailed experimental and theoretical studies demonstrate that despite complexities of struc-

(36) Bertini, L.; Stiewe, C.; Toprak, M.; Williams, S.; Platzek, D.; Mrotzek, A.; Zhang, Y.; Gatti, C.; Muller, E.; Muhammed, M.; Rowe, M. *J. Appl. Phys.* **2003**, *93*, 438–447.
(37) Dresselhaus, M. S.; Chen, G.; Tang, M. Y.; Yang, R. G.; Lee, H.; Wang, D. Z.; Ren, Z. F.; Fleurial, J. P.; Gogna, P. *Adv. Mater.* **2007**, *19*, 1043–1053.
(38) Rao, A. M.; Ji, X. H.; Tritt, T. M. *MRS Bull.* **2006**, *31*, 218.
(39) Zhou, M.; Li, J. F.; Kita, T. *J. Am. Chem. Soc.* **2008**, *130*, 4527–4532.
(40) Kim, W.; Zide, J.; Gossard, A.; Klenov, D.; Stemmer, S.; Shakouri, A.; Majumdar, A. *Phys. Rev. Lett.* **2006**, *96*, 045901.
(41) Callaway, J.; Von Baeyer, H. C. *Phys. Rev.* **1960**, *120*, 1149–1154.
(42) Yang, J.; Meisner, G. P.; Chen, L. *Appl. Phys. Lett.* **2004**, *85*, 1140–1142.

(43) The unit cell lattice parameter of $Na_{13}Pb_5SnBiTe_{20}$ is 6.412 Å, and there are 8 atoms, $\Omega = 32.95 \times 10^{-30}$ m^3/atom, θ_D= 135 K, $\nu = 2.23 \times 10^3$ m/s.

tures and behavior of multicomponent systems, tractable nanoscale structure analysis is feasible which can provide consistent insights in the correlative behavior of thermoelectric materials.

Acknowledgment. Financial support from the Office of Naval Research (N00014-08-1-0613) is gratefully acknowledged. Transmission electron microscopy work was performed in the (EPIC) (NIFTI) (Keck-II) facility of NUANCE Center at Northwestern University. NUANCE Center is supported by NSF-NSEC, NSF-MRSEC, Keck Foundation, the State of Illinois, and Northwestern University. Work at BNL was supported by the DOE Office of Science under Contract No. DEAC02-98CH10886.

JA905448B